



Deposited via The University of Sheffield.

White Rose Research Online URL for this paper:

<https://eprints.whiterose.ac.uk/id/eprint/97243/>

Version: Supplemental Material

Article:

Murray, T., Nettles, M., Selmes, N. et al. (2015) Reverse glacier motion during iceberg calving and the cause of glacial earthquakes. *Science*, 349 (6245). pp. 305-308. ISSN: 0036-8075

<https://doi.org/10.1126/science.aab0460>

Reuse

Items deposited in White Rose Research Online are protected by copyright, with all rights reserved unless indicated otherwise. They may be downloaded and/or printed for private study, or other acts as permitted by national copyright laws. The publisher or other rights holders may allow further reproduction and re-use of the full text version. This is indicated by the licence information on the White Rose Research Online record for the item.

Takedown

If you consider content in White Rose Research Online to be in breach of UK law, please notify us by emailing eprints@whiterose.ac.uk including the URL of the record and the reason for the withdrawal request.



1
2
3
4
5
6
7
8
9
10
11
12
13
14
15
16
17
18
19
20
21
22
23

Supplementary Materials for

Reverse Glacier Motion During Iceberg Calving and the Cause of Glacial Earthquakes

T. Murray, M. Nettles, N. Selmes, L. M. Cathles, J. C. Burton, T. D. James, S. Edwards, I. Martin, T. O'Farrell, R. Aspey, I. Rutt, and T. Baugé

correspondence to: t.murray@swansea.ac.uk

This PDF file includes:

Materials and Methods
Fig. S1

24 **Materials and Methods**

25

26 Glacial earthquake analysis

27

28 We detected glacial earthquakes by back-propagation of vertical-component seismic
29 signals recorded at stations of the global seismographic network (13, 23). We also
30 inspected back-propagated seismograms and array stacks interactively to identify
31 earthquakes too small for automatic detection by our standard algorithm (10). The
32 earthquakes were initially identified independently of image analysis; one additional
33 weak seismic signal was confirmed as an earthquake after comparison with camera
34 imagery.

35 We modelled the seismic waveforms using a centroid-single-force (CSF) formalism
36 (11, 25) to confirm earthquake locations and obtain earthquake source parameters
37 including the orientation of the force active during the earthquake, the earthquake CSF
38 amplitude, and the earthquake centroid time, t_c (centroid of the temporal force history).
39 The inversion approach and data processing follow ref. 6. We assume a force-time
40 history 50 s long in which the force has a constant amplitude for one half the earthquake
41 duration, followed by a constant amplitude of opposite polarity for the remainder of the
42 duration; that is, the time function is a square wave of one cycle. The centroid time
43 corresponds to the time of the polarity reversal of the force at the earthquake half
44 duration. We note that the force-time history used in the seismic inversions is not derived
45 from the seismic data, but is prescribed. The most important feature of the time function
46 for the current analysis is the rapid change in force amplitude that occurs at t_c . As
47 discussed in ref. 16, the true earthquake time function may not be symmetric, and may
48 have longer duration. Here, we choose to use the 50-s boxcar function for consistency
49 with previous systematic studies of glacial earthquakes (6, 10, 11, 13, 16).

50 We performed an experiment using the scaled force and pressure timeseries from the
51 laboratory experiments to provide input, time-varying force histories simulating a glacial
52 earthquake. The pressure timeseries were converted to a vertical force history by
53 multiplication by the map-view area of the iceberg calved, as determined from
54 photogrammetric analysis. Vertical and horizontal force histories were downsampled to
55 one sample every 10 s and modelled as a series of overlapping isosceles triangles of
56 varying height. Synthetic seismograms were calculated by summation of normal modes
57 in the preliminary reference Earth model (PREM) (26) for each triangular sub-source and
58 the seismograms summed to form the complete records. Seismograms were calculated for
59 stations at a range of distances and azimuths representative of those typically available
60 for analysis of glacial earthquakes at Helheim Glacier. The seismograms were then
61 inverted using the same approach as for data seismograms to obtain earthquake
62 parameters.

63

64 Photogrammetric analysis

65

66 Two 15.1 megapixel Canon 50D single lens reflex (dSLR) cameras were installed in
67 stereo configuration on the bedrock margins of Helheim Fjord ~4 km down-fjord (east)
68 from and looking at the calving front. The cameras were manually synchronized to take

69 hourly photographs and operated between 2013 DOY 196 and 245. Fixed 28 mm wide-
70 angle lenses were used in order to capture the majority of the calving front. Digital
71 elevation models (DEMs) were produced photogrammetrically from stereo imagery using
72 the 3D visualization capabilities of SocetSET digital photogrammetry suite alongside the
73 bundle adjustment and DEM extraction components of Topcon's ImageMaster. Ground
74 control information was extracted from a 2013 lidar DEM (27). We compared DEMs
75 prior to and following calving events to obtain three-dimensional calving geometry,
76 including the locations of the calving margins. Detailed methodology of the
77 photogrammetric processing is described in the Methods and Supplementary Material of
78 ref. 8.

79

80 Estimates of glacier thickness and iceberg aspect ratio

81

82 Estimates of glacier thickness for the DOY 206 and 212 events were made using
83 IceBridge MCoRDS L3 Gridded Ice Thickness, Surface, and Bottom, Version 2 (28).
84 Mean bottom elevations of flightline points that fell within the areal extent of each
85 calving event provided our estimates. In the vicinity of the heavily crevassed calving
86 front, errors are estimated to be ± 60 m (8).

87 Iceberg aspect ratios, defined as the along-flow width of the calved iceberg to the
88 estimated iceberg height, were estimated using the photogrammetric results and an
89 equivalent rectangular iceberg, together with the estimated glacier thickness. Idealized
90 rectangular dimensions were constructed by measuring iceberg cross-glacier and along-
91 flow widths and adjusting these to rectangular dimensions matching the measured map-
92 view area of ice lost in each calving event.

93

94 GPS data processing

95

96 GPS sensors on ice and bedrock used Ashtech MB100 dual-frequency geodetic
97 receiver boards and ASH111661 dual-frequency antennas.

98 The position of the base station located on bedrock was estimated using the Precise
99 Point Positioning (PPP) method (29) with GIPSY-OASIS version 6.2 software from JPL.
100 In addition to base-station coordinates and a receiver clock offset, a zenith wet
101 tropospheric delay and tropospheric gradients were estimated. JPL fiducial orbit and 30-s
102 clock products were held fixed. Hydrostatic zenith delay was modelled (30) with zenith
103 delays mapped to elevation using the Global Mapping Function (GMF) (31). Ocean tide
104 loading displacements were corrected for using the FES2004 model (32) and solid Earth
105 tides were corrected according to the IERS 2010 conventions (33). Carrier-phase
106 ambiguities were fixed to integers where possible (34).

107 GPS data from sensors on the glacier surface were processed using the relative
108 carrier-phase method with TRACK version 1.29 software (35) from GAMIT 10.50.
109 Kinematic positions were estimated with respect to the fixed base station using the
110 ionosphere-free linear combination of L1 and L2 observations (LC). Baseline lengths
111 ranged from 1.5-5.6 km. An elevation-angle cutoff of 10° was applied. We used orbit
112 and high-rate (5 s) clock products from CODE (36). Zenith delays were modelled and
113 mapped as above (30, 31) but no wet tropospheric correction was estimated. Observations
114 were processed on a day-of-year basis, with prior-day and following-day orbit and clock

115 data appended to facilitate TRACK's interpolation scheme. Kinematic site motion was
116 modelled using a random-walk stochastic model. The model standard deviation was set at
117 $0.01 \text{ m/s}^{0.5}$. Position time series were filtered to exclude data where the number of
118 unfixed biases was greater than 2, the number of double differences was fewer than 10, or
119 the height uncertainty was greater than 0.1 m.

120

121 Laboratory Experiments

122

123 *Data acquisition*

124

125 The laboratory experiments were performed in a fresh-water tank 244 cm long, 30
126 cm wide, and 30 cm tall, similar to tanks used previously (19, 24, 37). A model glacier
127 terminus was secured at one end of the tank. Plastic icebergs made from polyethylene
128 with a density nearly identical to glacier ice (920 kg/m^3) and height $H_L = 20.3 \text{ cm}$, width
129 ϵH_L , and cross-tank dimension $D_L = 26.7 \text{ cm}$ were placed flush against the terminus and
130 allowed to capsize spontaneously under the influence of gravitational and buoyancy
131 forces. Experiments were conducted with icebergs of aspect ratio $\epsilon = 0.22, 0.28, 0.43,$
132 0.54 . Three levels of perforated plastic sheet were secured at an incline to the water's
133 surface at the other end of the tank to damp seiche modes (38). Two different model
134 termini were used: one with an embedded pressure sensor that monitored pressure at
135 three water depths and one that was coupled to four force sensors located at each corner
136 of the terminus. The pressure and force data were acquired at a rate of 200 Hz.

137 The pressure sensor (GEMSTTM) had a maximum range of 2500 Pa hydrostatic
138 pressure and a response time of 5 ms. We used the pressure data recorded at the deepest
139 of the three measured depths in our analyses. The force sensors (Strain Measurement
140 Devices) each had a maximum range of 0.5 N. The sensors rely on mechanical deflection
141 to measure the force. The terminus used to measure the force was designed so that its
142 frequency response was flat in the bandwidth produced by the motion of the iceberg and
143 subsequent waves. The total force was calculated by summing the signals from all four
144 sensors and inherently represents a sum of contact and pressure forces acting on the
145 terminus. Repeat experiments showed nearly identical results for both the pressure and
146 force measurements. The results shown in Figure 3 represent the average of 3 force
147 measurements and 5 pressure measurements. The position and orientation of the plastic
148 iceberg were determined by image analysis and were used to synchronize the force and
149 pressure measurements in time.

150

151 *Scaling of laboratory data*

152

153 In order to compare lab data to field data, the forces and pressures measured in the
154 laboratory were scaled up to match the dimensions of icebergs at Helheim Glacier, as
155 measured by photogrammetry. Following previous studies (19, 24), the laboratory data
156 were scaled by powers of the ratio of the iceberg height in the field, H_F , to the iceberg
157 height in the laboratory, H_L . Because the gravitational potential energy released by
158 iceberg capsize scales as H^4 (24, 39), force measurements from the laboratory were
159 scaled by $(H_F/H_L)^3$, pressure measurements by (H_F/H_L) and time scales by $(H_F/H_L)^{1/2}$.
160 This method of scaling implicitly assumes that the flow of the water in the lab and in the

161 field can be considered dynamically similar. The Reynolds number for flow is $\sim 10^{10}$ in
162 the field and $\sim 10^5$ in the lab, but the flow is turbulent in both cases and typical drag
163 coefficients on solid bodies vary little in this flow regime (19, 24).

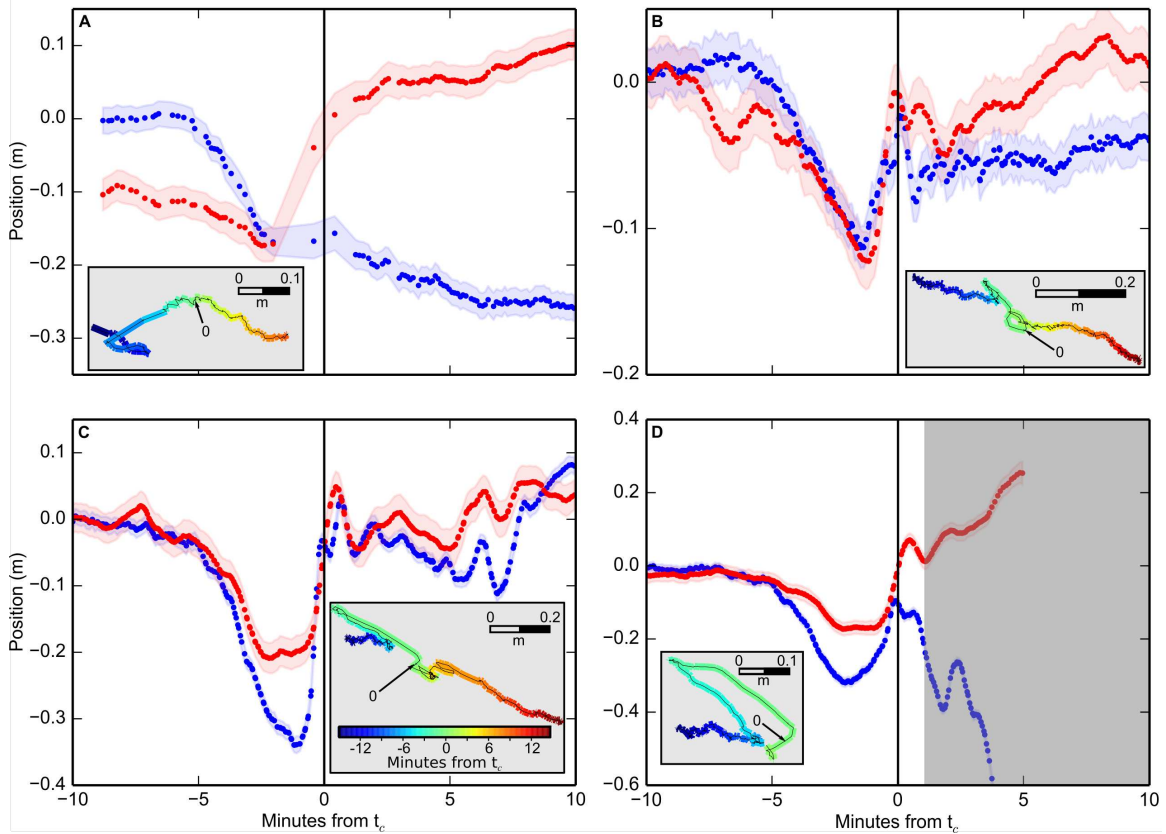
164 *Prediction of glacier deflection*

165
166
167 The scaled force and pressure are used to predict the time history of deflection of the
168 glacier-terminus region. We modeled the deflection of the calving region as an elastic
169 response to the force applied. The total force per unit area acting on the glacier terminus
170 produces a linear deflection orthogonal to the calving front such that $F_{\text{tot}}/A_F = E\Delta L/L$,
171 where E is the Young's modulus of glacial ice (~ 1 GPa; refs. 40, 41). The area over
172 which the total force acts is the surface area of the terminus adjacent to the capsizing
173 iceberg, $A_F \sim H_F D_F$, where D_F is the cross-glacier length of the calved iceberg. In Figure
174 3, the value of L was chosen so as to best match the GPS data ($L=4.9$ km). The length-
175 scale L likely represents the approximate distance from the terminus to the grounding
176 zone.

177 The pressure reduction in the water behind the rotating iceberg creates a downward
178 force on the front of the glacier (in contrast to the upward force it causes on the solid
179 earth). The water under the ungrounded region of the glacier responds to this reduction in
180 pressure ($\sim 5 \times 10^4$ Pa), creating a net vertical force acting on the glacier over an area A_P
181 $\sim \kappa L D_F$, where κ is the fraction of the length L over which the pressure is initially
182 reduced beneath the glacier. We model the glacier tongue as an Euler–Bernoulli beam of
183 length L with a varying load due to gravitational, buoyant, and pressure forces acting on
184 it. Our simplified model assumes the beam is clamped at the grounding line and stress
185 free at the terminus. Varying κ to match the L determined from the horizontal deflection
186 ($L = 4.9$ km) yields $\kappa = 0.02$, such that the pressure load is applied over a narrow region
187 parallel to the glacier terminus consistent with the dimensions of the capsizing iceberg.

188 For the comparison of predicted and observed deflection shown in Figure 3, we low-
189 pass filter the scaled pressure and force traces using a 5-pole Butterworth filter with a
190 corner period of 40 s. The pressure and force records are dominated by the very-long-
191 period deflection signal, and this choice of filtering does not affect our results or
192 interpretation, but serves to reduce the presence of high-frequency oscillations of the
193 water column in the tank that are expected to be damped by ice mélange in the glacier
194 fjord. It also removes low-amplitude, very-high-frequency sensor noise.

195 We find that the model iceberg aspect ratio for which the scaled laboratory data best
196 match the observed GPS data shown in Figure 2 is $\varepsilon = 0.22$, compared to a measured
197 iceberg aspect ratio from field data of 0.23.



200

201 **Fig. S1.**

202 **Additional examples of glacier response at times of glacial earthquakes.** (A) Sensor 6
 203 at 03:13 on DOY 206 2013; some data missing due to communications failure. (B)
 204 Sensor 15 at 03:13 on DOY 206 2013. (C) Sensor 1 at 12:56 on DOY 206 2013. (D)
 205 Sensor 15 at 12:56 on DOY 206 2013; sensor is lost shortly after this event. Symbols as
 206 in Figure 2. Horizontal displacement for B-D has trend of 30-10 mins before t_c removed
 207 (B=27.6 m/day, C=27.5 m/day, D=29.4 m/day) and for panel A the trend from 10-5 mins
 208 before t_c (36.0 m/day). Height has mean removed. Insets (grey boxes) show plan view of
 209 GPS trace during 30 minutes around t_c , marked as 0; in panel (D), grey shaded region
 210 (showing time of imminent sensor loss) in main panel is excluded from inset.